Bioelectrochemistry 138 (2021) 107733

Contents lists available at ScienceDirect

Bioelectrochemistry

journal homepage: www.elsevier.com/locate/bioelechem

Highly sensitive electrochemical detection of cancer biomarker based on anti-EpCAM conjugated molybdenum disulfide grafted reduced graphene oxide nanohybrid

Owais Jalil, Chandra Mouli Pandey *, Devendra Kumar *

Department of Applied Chemistry, Delhi Technological University, Delhi 110042, India

ARTICLE INFO

Article history:
Received 24 August 2020
Received in revised form 19 November 2020
Accepted 23 December 2020
Available online 29 December 2020

Keywords:
Cancer
Biomarkers
Biosensor
EpCAM
Graphene oxide
Molybdenum disulfide

ABSTRACT

An ultrasensitive, electrochemical biosensor has been fabricated by utilizing molybdenum disulfide (MoS_2) grafted reduced graphene oxide (MoS_2@rGO) nanohybrid as a sensing platform. Biomolecular-assisted synthetic method was adopted to synthesize MoS_2@rGO nanohybrid, where L-cys was used to reduce GO. The MoS_2@rGO nanohybrid exhibits improved electrochemical performance when it has been electrophoretically deposited onto the indium tin oxide (ITO) coated glass substrate. Further, epithelial cell adhesion molecule antibodies (anti-EpCAM) specific to cancer biomarker has been covalently immobilized on the MoS_2@rGO/ITO electrodes for label-free detection of EpCAM. Electrochemical results confirm that anti-EpCAM/MoS_2@rGO/ITO based biosensor can detect EpCAM in the concentration range of 0.001–20 ng mL^{-1} with a detection limit of 44.22 fg mL^{-1} (S/N = 3). The biosensor's excellent analytical performance has been attributed to the efficient immobilization of EpCAM antibodies on the MoS_2@rGO surface, which results in high specificity for EpCAM antigen. The fabricated biosensor showed good selectivity, reproducibility, and stability. The successful detection of EpCAM antigen in spiked samples (human saliva, serum and urine) makes this platform an alternative method for early screening of cancer biomarker.

1. Introduction

Cancer has been considered the second-largest disease with a high mortality rate where patient's survival is uncertain because of limited cancer diagnostic techniques [1]. The traditional techniques for detecting cancer mainly rely on the cell morphology detected using staining and microscopy, which is not sensitive enough [2]. However, accurate and effective methods are urgently needed for the successful detection and clinical diagnosis of cancer [3]. Recently, biomarker-based cancer diagnosis has shown significant potential in detecting and monitoring cancer patients [4]. These immunoassays are being widely used for sensitive and selective detection of cancer biomarkers, although they are time-consuming, expensive, and not sensitive enough to detect a lower concentration of biomarkers in the initial stages of cancer [5]. Moreover, being manual, these methods for biomarker detection are slow and consume expensive reagents in every assay [6]. Therefore, there is an urgency for sensitive and rapid technology, which will help in providing better healthcare by increasing sensitivity and reducing the waiting time.

Nowadays, biosensors play a critical role in determining cancer biomarkers as they are portable, easy to use, and can analyze in real-time [7,8]. Among the various biomarkers, epithelial cell adhesion molecule (EpCAM; glycosylated membrane protein) has been considered a prognostic tumor biomarker expressed in most cancer cells [9,10]. EpCAM has been found to be strongly expressed in carcinomas of various origins, such as breast, colorectal, lung, prostate, etc., and have critical clinical significance in the early monitoring of tumors, mainly in determining the different stages of cancer [11,12]. The detection of EpCAM using florescent, surface Plasmon resonance, and calorimetric based biosensor has shown promising results [6,13-15]. Moreover, a cost-effective biosensor with higher sensitivity and selectivity for timely and reliable detection of EpCAM is still required. In this context, electrochemical biosensors have shown huge potential because of its accuracy, ease of preparation, smooth operation, high sensing ability and selectivity [16]. However, when the concentration of the target molecule is very low, the signal generated during the biochemical reaction is too weak and may not be detected by the conventional electrode [17,18]. So, electrode material should be designed in such a way

* Corresponding authors.
E-mail addresses: cmp.npl@gmail.com (C.M. Pandey), dkumar@dce.ac.in (D. Kumar).

https://doi.org/10.1016/j.bioelechem.2020.107733
1567-5394/

that it can amplify the electrochemical signals resulting in high sensitivity. In this context, electrochemical biosensors based on transition metal dichalcogenides, especially Molybdenum disulfide (MoS_2), are being widely explored because of their tunable bandgap, enhanced electrical, optical and thermal properties [19-22]. However, the major problem in using bare MoS_2 is the sheet's restacking, which minimizes the surface energy leading to low intrinsic conductivity [23,24]. This limitation may be reduced by integrating MoS_2 with graphene oxide (GO) as both GO and MoS_2 have similar layered structures and morphology [25,26]. The hybridization of MoS_2 and GO have a synergetic effect, which ascends from the retention of adequate carrier mobility [27,28]. The integration may enhance the electrochemical properties and provide biocompatibility to the desired biomolecules [22,29].

Considering the perspective of MoS_2@rGO nanohybrid in the fabrication of biosensors, efforts have been made to utilize these nano-entities as a sensing platform for the development of biosensor for EpCAM detection. The MoS_2@rGO nanohybrid was synthesized using biomolecular-assisted synthetic methods where L-cysteine (L-cys) has been used. L-cys not only provides multifunctional groups for the conjugation of the anti-EpCAM but also acts as a reducing agent, which results in the formation of MoS_2@rGO nanohybrid during the hydrothermal process [26,30]. Moreover, the enhanced surface area of MoS_2@rGO nanohybrid increases the diffusion of the redox ions, which leads to improved electron kinetics.

2. Materials and method

2.1. Chemicals and reagents

Graphite powder (<20 μm), ammonium molybdate ($(NH_4)_6Mo_7O_{24}{\cdot}4H_2O$, ≥99.0%), magnesium nitrate ($Mg(NO_3)_2$), L-Cysteine (L-cys), N-ethyl-Ń-(3-dimethyl aminopropyl) carbodiimide (EDC), N-hydroxysuccinimide (NHS), and the other reagents and solvents have been procured from Sigma-Aldrich, India. Monoclonal antibodies (anti-EpCAM) and the antigen (EpCAM) were procured from Sigma-Aldrich, USA. Deionized (DI) water (Mill-Q, Millipore, 18.2 MΩ cm) was used for preparing the solutions and all the solutions and glass-wares were autoclaved before use.

2.2. Synthesis of GO and rGO

The synthesis of GO from graphite powder has been previously reported [31,32]. The synthesized GO has been reduced by adding 0.6 g of L-cys into 40 mL of GO aqueous solution (0.5 mg mL^{-1}) and the solution was stirred for 10 h (27 °C) [33]. The obtained black product has been separated by centrifuging the solution at 9000 rpm followed by washing with DI water (3–4 times) to remove surplus L-cys. The obtained rGO was dried in a vacuum oven at 100 °C for 12 h and stored in a desiccator at room temperature.

2.3. Synthesis and functionalization of MoS_2@rGO nanohybrid

The biomolecular-assisted synthetic route has been used for synthesizing the MoS_2@rGO nanohybrid [26]. The prepared GO was added in 60 mL of DI water, followed by the addition of 0.5 g of $(NH_4)_6Mo_7O_{24}{\cdot}4H_2O$. The solution was ultrasonicated and stirred for about 45 min. The solution pH was maintained at 6.5 by adding NaOH (0.1 M) to the solution. Further, at this pH, L-cys (2.0 g) was added and the solution was kept in a Teflon-lined stainless steel autoclave (100 mL), which was heated at 240 °C for 12 h. After cooling the autoclave, the black precipitate obtained was centrifuged, washed using DI water: ethanol (2:1), and vacuum dried in the oven at 90 °C for 12 h (Fig. 1A).

2.4. Electrophoretic deposition (EPD) of MoS_2@rGO nanohybrid and biosensor fabrication

The synthesized nanohybrid was deposited electrophoretically on a pre-cleaned ITO coated glass substrate. For EPD, platinum has been used as a counter electrode, which was placed 0.5 cm apart from the ITO electrode. Before deposition, the colloidal suspension of MoS_2@rGO nanohybrid was sonicated in DI water and ethanol (1:5). The EPD was carried out by applying a DC potential (15 V) for 25 sec. For the smooth deposition, magnesium nitrate (10^{-4} M) was used, which gets absorbed onto the MoS_2@rGO nanohybrid, thus creating a positive surface charge [34].

For the immobilization of antibodies, the MoS_2@rGO/ITO electrodes were incubated (1 h) with 5 mM NHS (15 μL) and 2 mM EDC (15 μL) and kept at room temperature (25 °C). Then 20 μL (60 μg mL^{-1}) of monoclonal anti-EpCAM was drop-casted onto the activated electrode. The different stages involved in the fabrication of EpCAM based biosensors have been illustrated in Fig. 1B.

2.5. Characterization

Bruker D-8 Advance X-ray diffractometer with monochromatic (Cu Kα), radiation was used to record the X-ray diffraction (XRD). Fourier transforms infrared (FT-IR) spectroscopy (Perkin-Elmer spectrometer; Model Spectrum BX) was used to investigate the formation of MoS_2@rGO nanohybrid. The FTIR measurements (400–4000 cm^{-1}) were obtained by averaging 32 scans. The thermogravimetric analysis (TGA; Perkin-Elmer 4000) was used to analyze the thermal degradation of MoS_2@rGO in the range of 25 to 900 °C (10 °C/min) in a nitrogen environment. Transmission electron microscopy (TEM, Hitachi Model, H-800) was used for the morphological analysis of MoS_2@rGO nanohybrid. Field-emitting scanning electron microscope (FESEM) studies were carried out to study the surface morphology of MoS_2@rGO/ITO electrodes and rGO/ITO electrodes. Electrochemical studies were carried out using Autolab potentiostat/galvanostat (Eco-Chemie, Netherlands) in phosphate buffer saline (PBS, 100 mM, pH 7.4, 0.9% NaCl) containing 5 mM $[Fe(CN)_6]^{3-/4-}$. For the electrode assembly, Ag/AgCl was used as a reference electrode, while platinum as an auxiliary electrode.

3. Results and discussion

3.1. Characterization of MoS_2@rGO nanohybrid

The XRD plot of bulk MoS_2 exhibits sharp and strong peaks and the corresponding planes at 2θ = 14.35° (0 0 2), 32.67° (1 0 0), 39.66° (1 0 3), 49.74° (1 0 5), and 58.60° (1 1 0) (Fig. 1C, curve i) [35]. Whereas, in the diffraction pattern of MoS_2@rGO nanohybrid, the diffraction peaks at 14.35°, 32.67°, and 58.60° have been only observed, showing the poor crystallinity of MoS_2 (curve iii). This poor crystallinity of MoS_2 is because of the integration of rGO that inhibits the layered MoS_2 growth occurring in the hydrothermal process [26]. After the formation of the MoS_2@rGO nanohybrid, the other peaks at 14.25°, 39.66°, and 49.74° disappeared. Although the peak intensity at 14.25°, corresponding to the (0 0 2) diffraction plane, decreased drastically in MoS_2@rGO nanohybrid (curve iii). This decrease in the peak intensity is perhaps due to the presence of rGO (curve ii), which hinders the growth of the MoS_2 crystal layer. From the XRD results, it can be inferred that during the hydrothermal process, L-cys reduces the Mo precursor to MoS_2, and GO was *in-situ* reduced to rGO [36]. The diffraction peak at 2θ ≈ 25° was hardly observed, showing that the graphene nano-

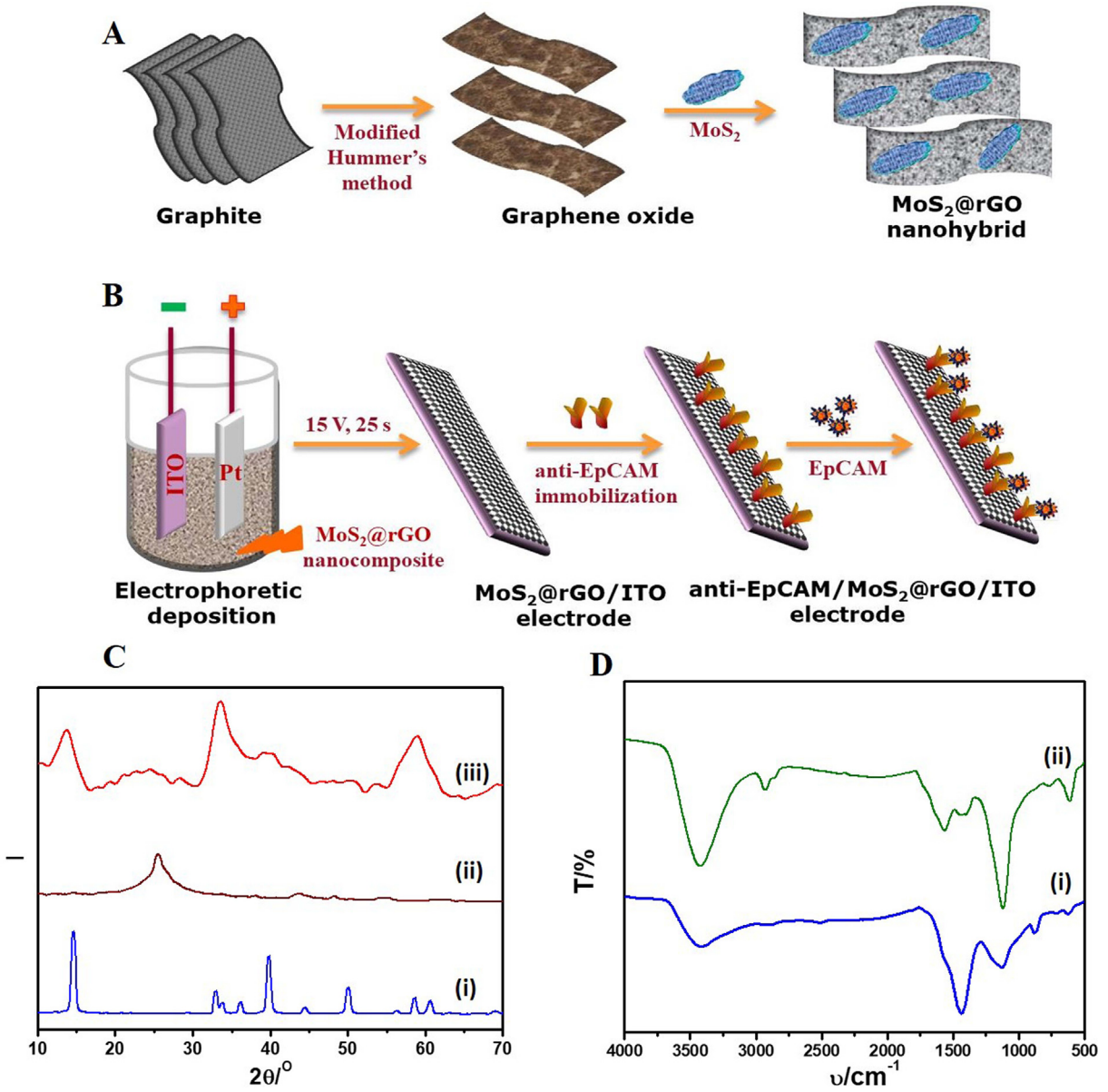

Fig. 1. Schematic description for the (A) synthesis of MoS_2@rGO nanohybrid and (B) fabrication of rGO@MoS_2/ITO based biosensor. (C) XRD patterns of (i) MoS_2, (ii) rGO and (iii) MoS_2@rGO nanohybrid. (D) FTIR spectra of (i) rGO and (ii) MoS_2@rGO nanohybrid.

sheets were not stacked together [37]. This could be because of layered MoS_2, which inhibits the stacking of rGO.

The FTIR spectra of GO show a broad peak at 3412 cm^{-1}, which is attributed to the stretching mode of the O-H bond. A peak at 1704 cm^{-1} arises due to the carboxyl group present on graphene. Another peak at 1634 cm^{-1} can be assigned to the stretching and bending vibration of water molecules. The peak at 1373 cm^{-1} is due to the presence of the C—OH group, while the other peaks at 1221 and 1064 cm^{-1} correspond to the stretching and vibrational modes of the C—O group, respectively [38,39] (Fig. S1A). After the reduction of the GO (Fig. 1D; curve i) and the formation of the MoS_2@rGO nanohybrid, there was a sharp decline in the peak intensity of the oxygen-rich functional groups suggesting the successful reduction of Mo precursor to MoS_2 and GO to rGO. The peak observed at 603 cm^{-1} in the spectra of MoS_2@rGO nanohybrid is attributed to the Mo–S vibration (Fig. 1D; curve ii) [39].

The thermal stability of MoS_2@rGO was confirmed using TGA (N_2 condition, 10 °C/min) (Fig. S1B). TG curves of MoS_2@rGO nanohybrid show continuous weight loss from initial temperature and show three stages of decomposition. The evaporation of absorbed H_2O molecules caused the first stage of weight loss at around 100 °C while the loss of weight around 350 °C was due to the thermal decomposition of the organic surface group, i.e., oxidation of MoS_2 into MoO_3. The drastic weight loss at 500 °C is because of the oxidation of MoS_2. After 700 °C, there was a gradual decrease in the TG curve showing a decrease in nanohybrid stability [40].

TEM analysis has been carried out to study the morphology of rGO and MoS_2@rGO nanohybrid. The TEM image of rGO shows a crumpled morphology where the lateral size of the individual graphene sheets is quite large (Fig. S2A). The TEM image of MoS_2@rGO nanohybrid exhibits a flower-like architecture constituted by exfoliated nano-sheets, where the MoS_2 nanostructures are well adhered on the rGO surface (Fig. 2A) [36]. The diameter of petal-like MoS_2 nano-sheets is in the range of ~200–300 nm having an average thickness of ~10 nm (Fig. 2B). Clear lattice fringe with an inter-planar spacing of 0.61 nm corresponding to 002 plane of

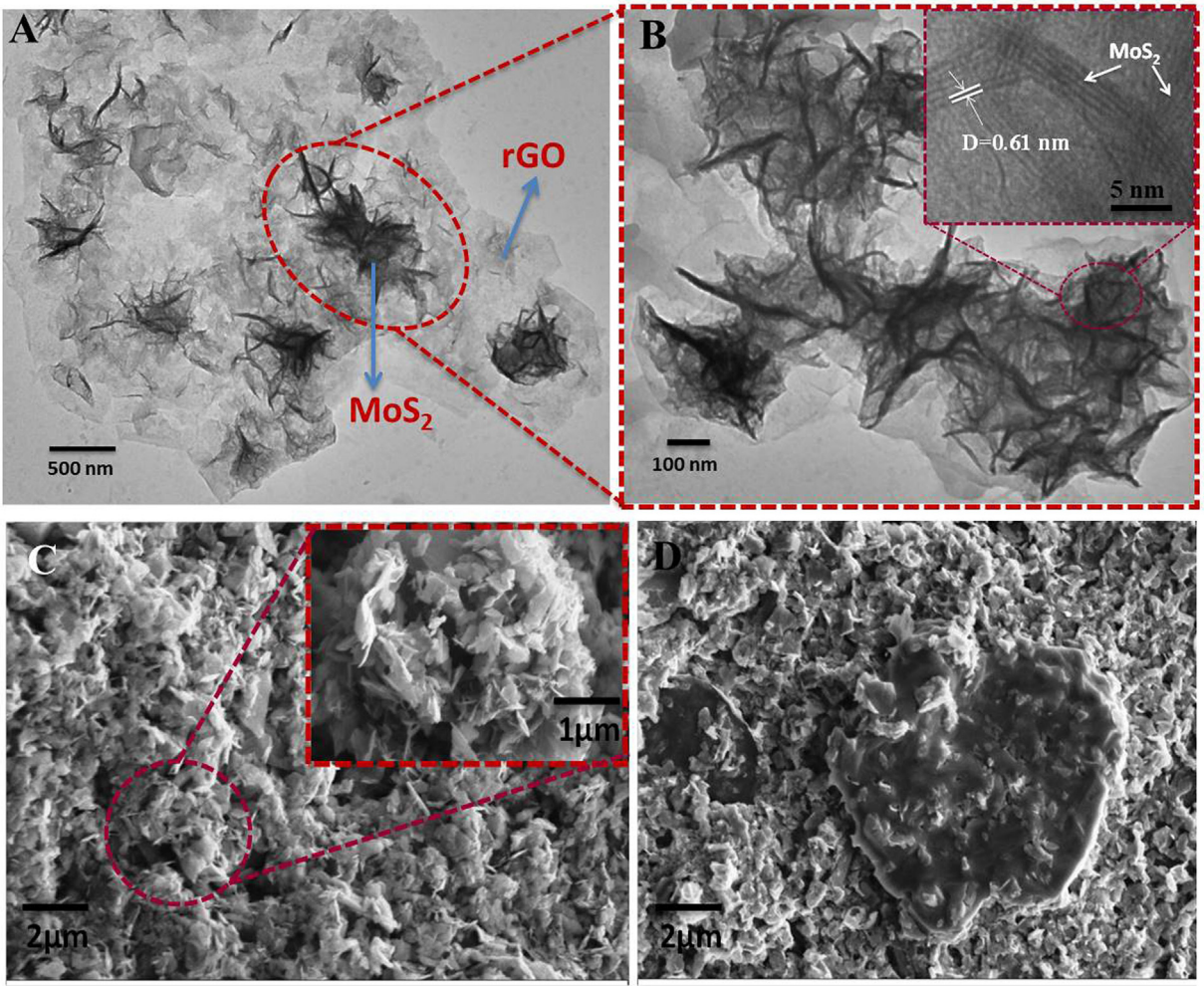

Fig. 2. TEM image of (A & B) MoS_2@rGO nanohybrid. SEM images of (C) MoS_2@rGO/ITO electrode, and (D) anti-EpCAM/ MoS_2@rGO/ITO electrode.

MoS_2 was observed in the HRTEM of one of the edges of MoS_2 (Fig. 2B, inset).

The SEM image of the rGO/ITO electrode shows the uneven distribution of rGO sheets onto the electrode surface (Fig. S2B), while the SEM micrograph of MoS_2@rGO nanohybrid shows 3D hierarchical structures (Fig. 2C). It has been observed that MoS_2 - nanoflowers like morphology are made up of nano-sheets that are anchored on rGO, resulting in the development of 3D hierarchical assembly. After immobilizing anti-EpCAM on the MoS_2@rGO/ITO electrode, the nanohybrid's structural morphology has been changed, confirming that the MoS_2@rGO/ITO electrode surface has been covered by anti-EpCAM (Fig. 2D).

3.2. Electrochemical characterization of the electrodes

Electrochemical impedance spectroscopy (EIS; frequency range 0.01–10^5 Hz) was used to study the electrochemical properties of the different modified electrode (Fig. 3A). The Nyquist plot consists of a semicircle portion (higher frequencies) and a linear region (lower frequencies) corresponds to electron transfer resistance limited process and diffusion-controlled electron transfer process, respectively [41]. The increase in the semicircle diameter implies the enhancement of electron transfer resistance (R_{ct}) that can be numerically derived from Randles and Ershler's equivalent circuit model [42]. The equivalent circuit (Fig. 3A (inset)) consists of an electron transfer resistance (R_{ct}), solution resistance (R_s), constant phase element (*CPE*), and Warburg impedance (Z_w) [43]. In the circuit, double-layer capacitance has been replaced by the CPE component because of the imperfect capacitance arising due to the electrode surface heterogeneity. The R_{ct} of MoS_2@rGO/ITO electrode (curve (i); 660.21 Ω ± 1.2) was found to be lower as compared with rGO/ITO electrode (curve iii; 1306.16 Ω ± 2.8). This may be attributed to MoS_2 and GO synergetic effect that enhances the electrochemical performance of the MoS_2@rGO/ITO electrode. The R_{ct} value of MoS_2@rGO/ITO electrode increases after the immobilization of anti-EpCAM (996.86 Ω ± 1.7; curve (ii)), which is due to the hindrance of the charge transfer by the non-conducting antibodies. After the incubation of the EpCAM to anti-EpCAM/ MoS_2@rGO/ITO electrode, the R_{ct} was further increased (curve (iv); 1589.29 Ω ± 2.6) due to the formation of antibody-antigen complex that acts as a barrier by hindering the diffusion of the $[Fe(CN)_6]^{3-/4-}$ to the anti-EpCAM/MoS_2@rGO/ITO electrode [44]. From the obtained R_{ct} values, the exchange current per geometric unit area (i_o) and the apparent electron transfer rate constant (K_{app}) for the different electrodes have been calculated using Eqs. (1) and (2), respectively:

$$i_o = nRT/R_{ct}F \quad (1)$$

$$K_{app} = RT/n^2F^2AR_{ct}C \quad (2)$$

where, R is the gas constant, n is the number of electrons transferred, F is the Faraday's constant, A is the area of the electrode, T

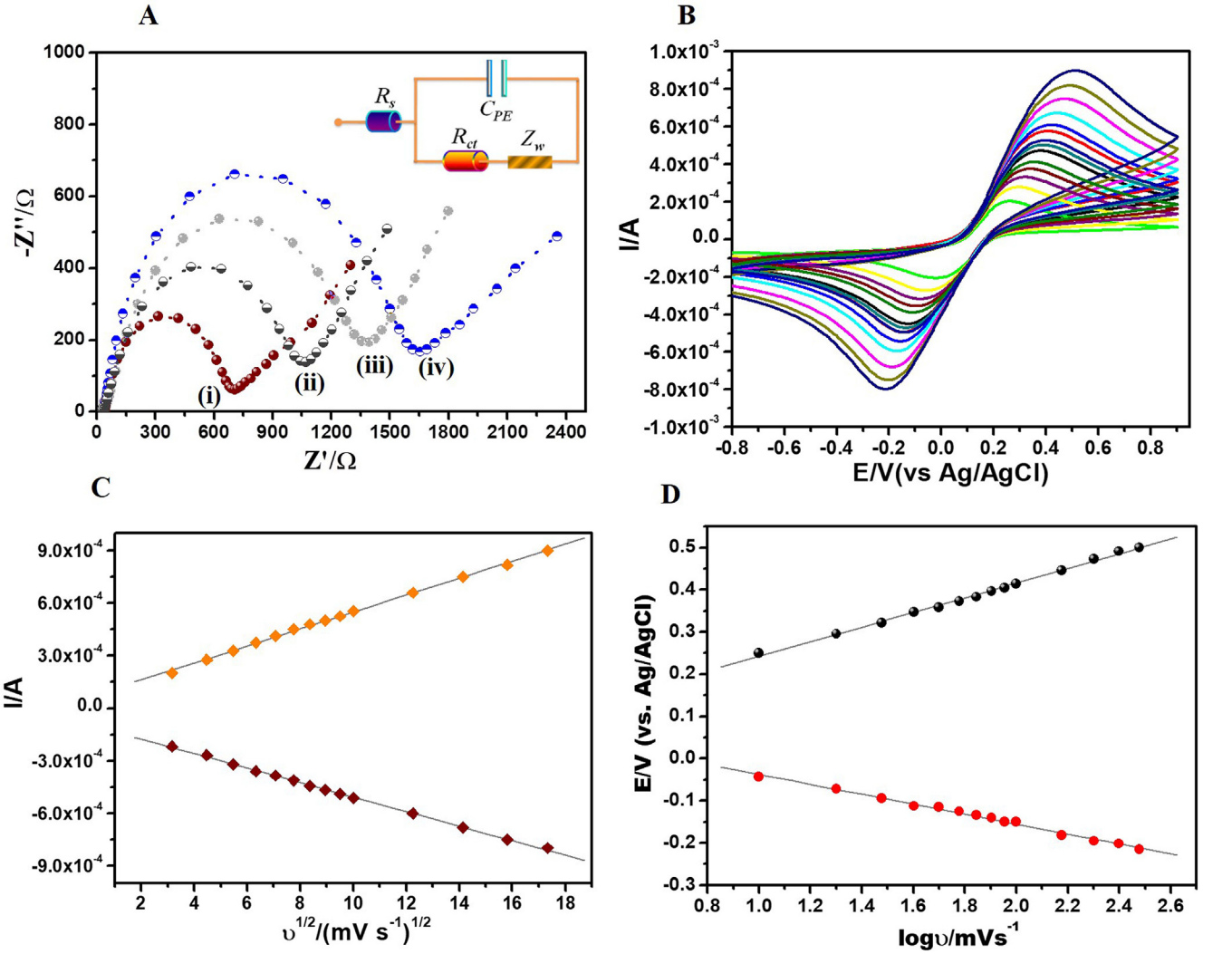

Fig. 3. (A) EIS plot for (i) MoS_2@rGO/ITO electrode (ii) anti-EpCAM/MoS_2@rGO/ITO electrode (iii) rGO/ITO electrode and (iv) anti-EpCAM/MoS_2@rGO/ITO electrode treated with EpCAM (B) CV analysis of MoS_2@rGO/ITO electrode with varying scan rate (10–300 mV). Plots of (C) I_{pa}, I_{pc}, vs. square root of scan rate and (D) potential with log of υ for MoS_2@rGO/ITO electrode.

is the temperature in Kelvin and *C* is the concentration of the redox probe. The i_o for MoS_2@rGO/ITO electrode was found to be 15.29×10^{-5} A cm^{-2}, whereas, after anti-EpCAM immobilization, i_o decreased to 10.13×10^{-5} A cm^{-2}. Similarly, the K_{app} for the MoS_2@rGO/ITO and anti-EpCAM/MoS_2@rGO/ITO electrode was calculated to be 4.032×10^{-7} cm s^{-1} and 2.135×10^{-7} cm s^{-1}, respectively. The reduction in i_o and K_{app} value for the anti-EpCAM immobilized MoS_2@rGO/ITO electrode is due to sluggish diffusion of the redox ions through the electrode interface.

Cyclic voltammetry (CV) analysis has been carried out by varying the scan rate (υ) from 10 to 300 mV s^{-1} in PBS containing 5 mM $[Fe(CN)_6]^{3-/4-}$ (Fig. 3B). The results reveal the linear relationship of peak current to the square root of the scan rate for the MoS_2@rGO/ITO electrode showing that the transfer of electron in MoS_2@rGO/ITO electrode is a surface-controlled process and follows Eqs. (3) & (4) (Fig. 3C). Furthermore, it was observed that with an increase in the υ (10–300 mV s^{-1}), there was an increase in the oxidation peak and the reduction peak. This suggests that the peak potentials are linearly dependent on the log υ (Eqs. (5) & (6)) (Fig. 3D).

$$I_{pa}[MoS_2@rGO/ITO] = 65.707\mu A + 48.370\mu A\,(s/mV) \times \upsilon(mV/s);\ R^2 = 0.9992 \quad (3)$$

$$I_{pc}[MoS_2@rGO/ITO] = -93.250\mu A - 41.406\mu A\,(s/mV) \times \upsilon(mV/s);R^2 = 0.9995 \quad (4)$$

$$E_{pa}[MoS_2@rGO/ITO] = 0.0685\ (V) + 0.1734(V) \times Log\ [\upsilon(mV/s)];R^2 = 0.9982 \quad (5)$$

$$E_{pc}[MoS_2@rGO/ITO] = 0.0806(V) - 0.1178(V) \times Log[\upsilon(mV/s)];R^2 = 0.9968 \quad (6)$$

Based on the above linearity curves and Randle Sevick equation (Eq. (7)), the diffusion coefficient (D) calculated for the MoS_2@rGO/ITO electrode was 3.19×10^{-6} cm^2 s^{-1}.

$$I_p = \left(2.99 \times 10^5\right)\alpha^{1/2}n^{3/2}ACD^{1/2}\upsilon^{1/2} \quad (7)$$

Here C is the molar concentration of $[Fe(CN)_6]^{3-/4-}$, and A is the electrode area.

3.3. Optimization of biosensing parameters for efficient bioelectrode response

The different biosensing parameters were optimized for the optimal bioelectrode response that governs the efficient detection of EpCAM. The optimal concentration required for the binding of the anti-EpCAM on MoS_2@rGO/ITO was estimated using DPV. The different concentration of anti-EpCAM was covalently immobilized on the MoS_2@rGO/ITO using EDC-NHS as the linker. There was a decrease in the DPV peak current on subsequent addition of anti-EpCAM in the concentration range 10–80 μg mL^{-1} and reached a plateau at EpCAM concentration at 60 μg mL^{-1} (Fig S3A). So, for the fabrication of the immunosensor, 60 μg mL^{-1} of anti-EpCAM concentration has been used. The performance of the biosensor is also affected by the pH of the electrolytic solution. So, the DPV studies of the anti-EpCAM/MoS_2@rGO/ITO electrode towards EpCAM (10 ng mL^{-1}) were measured at different pH values (5.4 to 9.4). The highest response current was obtained at pH 7.4, showing that this is the ideal pH condition for biosensing studies (Fig S3B). The time for the incubation of EpCAM on the anti-EpCAM/MoS_2@rGO/ITO electrode surface was studied by varying the incubation time from 0 to 15 min (Fig S3C). It was observed that the DPV current gets saturated after 10 min showing that maximum binding was achieved during this time.

3.4. Electrochemical biosensing response studies of anti-EpCAM/MoS_2@rGO/ITO electrode

Biosensing studies of the anti-EpCAM/MoS_2@rGO/ITO electrode were examined in the presence of varying EpCAM antigen concentrations in the range 0.001–20 ng mL^{-1}. Fig. 4A shows a linear decrease in the anodic peak current when the concentration of EpCAM was increased from 0.001 to 20 ng mL^{-1}. The increase in the concentration of EpCAM on the anti-EpCAM/MoS_2@rGO/ITO electrode surface results in the development of insulating layers that hinders the transport of electrons, causing a decrease in peak current. The slope of the calibration plot vs. the concentration of EpCAM shows a good linear relationship between the current response and the different EpCAM concentrations (Fig. 4B). The sensitivity (slope/surface area) of the biosensor has been calculated from the regression equation (I_p = 0.412 mA–0.026 mA/ng/mL × E pCAM concentration ng/mL) and was found to be 0.104 mA ng^{-1} mL cm^{-2} with R^2 of 0.9985. The limit of detection was estimated to be 44.22 ± 0.21 fg mL^{-1} using the equation 3σ/S, where σ is the standard deviation of the bioelectrode and *S* is the sensitivity that has been obtained from the slope of the calibration curve. Compared to the other EpCAM based biosensor reported in the literature, the obtained LOD for the fabricated biosensor is significantly low (Table 1) [6,13–15]. This may perhaps be due to the

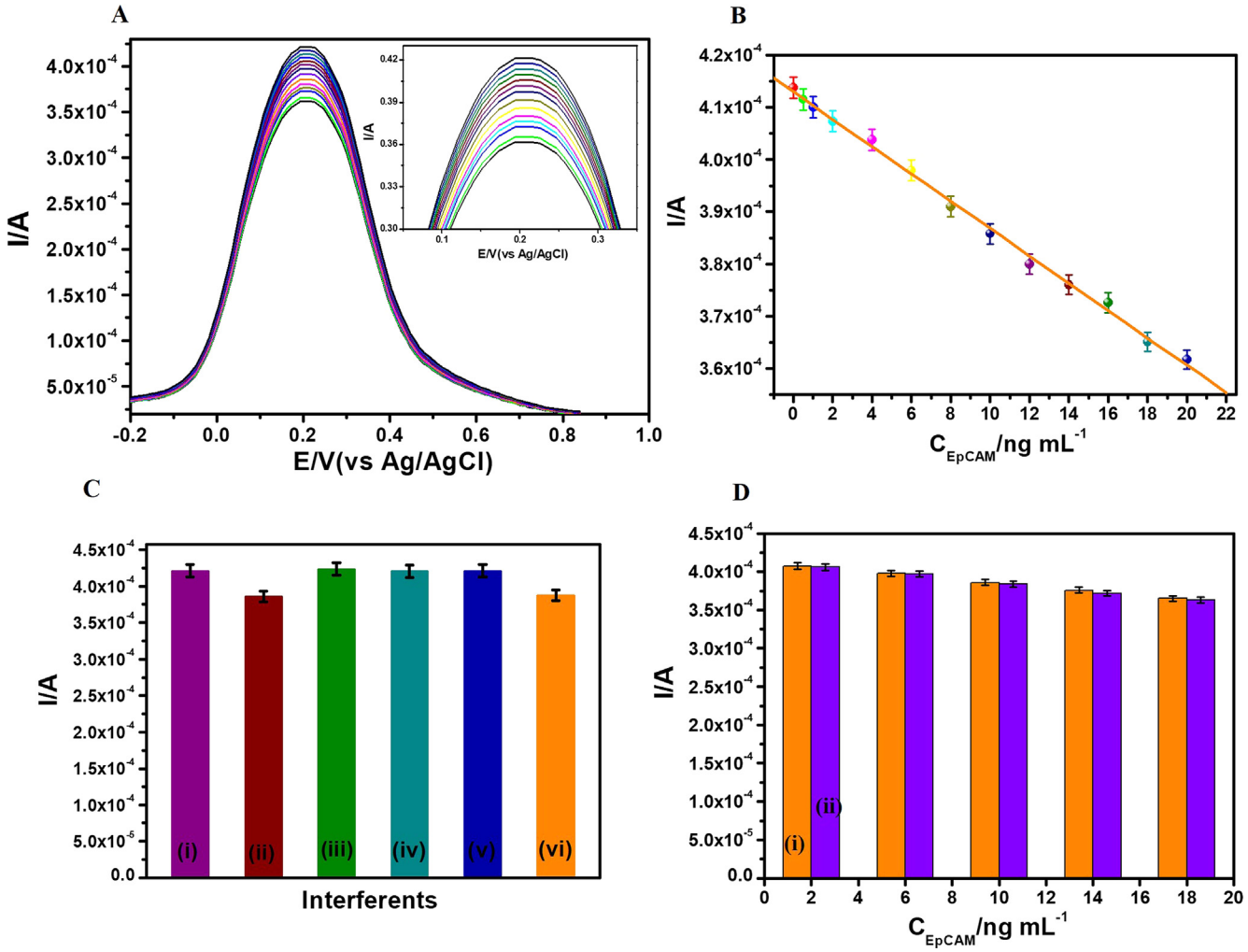

Fig. 4. DPV studies showing the response of the (A) anti-EpCAM/MoS_2@rGO/ITO electrode as a function of EpCAM concentration (0.001–20 ng mL^{-1}); inset is the magnified view of peak current for different concentrations of EpCAM, (B) Calibration plot between the magnitudes of current recorded and concentration of EpCAM (0.001–20 ng mL^{-1}). (C) Specificity studies of the (i) anti-EpCAM/MoS_2@rGO/ITO electrode with (ii) EpCAM (iii) glucose (iv) NaCl, (v) IgG (vi) EpCAM + other interferents. (D) Electrochemical response of the biosensor in (i) buffer sample and (ii) spiked human serum sample.

Table 1
Bio-sensing characteristics of MoS_2@rGO/ITO electrode along with other immunosensor reported in the literature for EpCAM detection.

S.No	Immobilization matrix	Detection technique	Linear detection range	Detection limit	Labeling	Ref.
1.	Rubpy core–shell Silica	Fluorescence & FCM	–	–	Yes	[14]
2.	GRs-QDs	ASV	100 fg mL^{-1} _7.5 μg mL^{-1}	100 fg mL^{-1}	Yes	[15]
3.	LC-SPDP/Au	CV and Fluorescence	$1x10^5$ – $1x10^8$ cells mL^{-1}	$1x10^5$ cells mL^{-1}	Yes	[6]
4.	AgNPs-PVA	EM	2–2000 pg mL^{-1}	0.8 pg mL^{-1}	No	[48]
5.	rGO@TiO_2/ITO	DPV	0.01–60 ng mL^{-1}	6.5 pg mL^{-1}	No	[34]
6.	MoS_2@rGO/ITO	DPV	0.001–20 ng mL^{-1}	44.22 fg mL^{-1}	No	Present work

Abbreviation: MoS_2: molybdenum disulfide, LC-SPDP: succinimidyl 6-(3-[2-pyridyldithio]-propionamido) hexanoate, Au: gold, Rubpy: tris(bipyridine)ruthenium(II)chloride, GRs: graphene oxide nano-sheets, QDs: quantum dots, AgNPs-PVA: silver nanoparticles covered with polyvinyl alcohol; ASV: Anodic stripping voltammetry, EM: electrochemical microfluidic.

Table 2
Recoveries of EpCAM spiked to different samples.

Sample	EpCAM added (ng mL^{-1})	EpCAM found (ng mL^{-1})	Recovery (100%)	RSD (%)
Buffer	10	9.98	99.8	4.2
Saliva	10	9.12	91.2	8.7
Serum	10	9.58	95.8	6.5
Urine	10	9.62	96.2	5.4

hierarchical structure of MoS_2@rGO nanohybrid that provides higher surface area resulting in enhanced electronic as well as electrochemical properties. Moreover, the enhanced sensing results of this biosensor can be assigned to the robust hybrid structure of MoS_2 and rGO resulting in the synergetic effects. The presence of rGO acts as an efficient electron promoter, while the MoS_2 has increased the loading of anti-EpCAM, leading to the increased interaction between EpCAM antigen and the antibodies [45].

3.5. Selectivity, reusability and shelf-life studies

The cross-reactivity of the fabricated biosensor against other biomolecules co-existing with EpCAM was estimated by analyzing its electrochemical performance in the presence of glucose, immunoglobulin G (IgG), sodium chloride (NaCl), and the mixture of interferents (Fig. 4C). Negligible change in the peak current has been observed when the biosensor was incubated with glucose, IgG and NaCl. Whereas, a decrease in current was observed when the bioelectrode was exposed to a mixture of EpCAM and other analytes. The obtained peak current was similar to that of the EpCAM interaction with the anti-EpCAM/MoS_2@rGO/ITO electrode. Based on these results, the selectivity coefficient (K_{sel}) was calculated to study the interference effect using Eq. (8) and for all the interferents the value of K_{sel} is found to be ~1[46].

$$K_{sel} = \frac{Signal_{interferent}}{Signal_{EpCAM}} \quad (8)$$

The biosensor's reusability and shelf-life are two essential parameters for determining the performance of biosensors in real biological samples. The reusability of the fabricated biosensor was investigated by dipping the electrode in urea solution (5 M) at a temperature of 37 °C for 5 min and then rinsed with Tris- HCl buffer (10 min). The results obtained for the different regeneration cycles indicate that the biosensor shows excellent regenerability and can be reused over 4 times (Fig. S4A). The shelf-life of the biosensor was estimated by measuring the DPV response of bioelectrodes (3 sets) towards EpCAM (10 ng mL^{-1}) after every 5 days duration (Fig. S4B). There was a negligible change in the current response compared to the initial current response (RSD < 4.2% (n = 3)), showing the satisfactory stability of the fabricated biosensor up to 45 days when stored at 4 °C.

3.6. Validation of the biosensor with human serum samples

The application and validation of the MoS_2@rGO/ITO based biosensor in biological samples (human serum, urine, and saliva) were studied by spiking the samples with EpCAM. The serum samples were collected under the protocol approved by the Rajiv Gandhi Cancer Institute and Research Centre (RGCIRC). For preparing the solutions, 300 μL of biological samples have been spiked with 10 ng mL^{-1} of EpCAM antigen (20 μL). Before the analysis, the human biological samples were diluted with the buffer solution. A decrease in the peak current was observed when the biosensor was incubated with the spiked biological sample. However, for the blank biological samples (non-spiked) the peak current observed was nearly similar to that of anti-EpCAM/MoS_2@rGO/ITO electrode [47]. The % recoveries calculated for the spiked samples were found to be in the range 91.2 to 99.8% with RSD of < 8.7% (n = 3) (Table 2).

For determining the potential of anti-EpCAM/MoS_2@rGO/ITO electrode in clinical applications, its electrochemical response has been measured with spiked human serum samples with different EpCAM concentrations (2–18 ng mL^{-1}). Fig. 4D indicates that there was a continuous decrease in the response current with increasing concentration of EpCAM. As shown in Table ST1, satisfactory recoveries have been observed with the spiked human serum sample with RSD < 5.4% (n = 3). Based on the above results, it may be inferred that the fabricated MoS_2@rGO based biosensor is reliable and can have an application in the early detection of cancer biomarker's.

4. Conclusions

We report a facile and environment-friendly route for synthesizing MoS_2@rGO nanohybrid, using the amino-acid assisted solution-phase method. The structural and morphological characterization indicates the 3D morphology of MoS_2@rGO nanohybrid, where MoS_2 was grafted on the rGO surface during the hydrothermal reaction. This MoS_2@rGO nanohybrid-based novel sensing platform shows reasonable detection limit, stability and reusability. The electrochemical analysis performed with the spiked samples compared with the standard samples indicates that this biosensor can potentially screen other cancer biomarkers.

CRediT authorship contribution statement

Owais Jalil: Conceptualization, Methodology, Data curation, Formal analysis, Writing - original draft. **Chandra Mouli Pandey:** Supervision, Investigation, Validation, Writing - review & editing, Project administration, Funding acquisition. **Devendra Kumar:** Supervision, Validation, Writing - review & editing.

Declaration of Competing Interest

The authors declare that they have no known competing financial interests or personal relationships that could have appeared to influence the work reported in this paper.

Acknowledgments

C.M. Pandey acknowledges Department of Science and Technology (DST), New Delhi, India, for the DST-INSPIRE Faculty award (Grant No. DST/INSPIRE/04/2015/000932). We extend our thanks to Prof. B. D. Malhotra (DTU) and Dr. Birendra K. Yadav (RGCIRC, New Delhi) for their valuable discussions.

Appendix A. Supplementary material

Supplementary data to this article can be found online at https://doi.org/10.1016/j.bioelechem.2020.107733.

References

[1] M. Arbyn, E. Weiderpass, L. Bruni, S. de Sanjosé, M. Saraiya, J. Ferlay, F. Bray, Estimates of incidence and mortality of cervical cancer in, a worldwide analysis, LancetGlob. Health 8 (2020) (2018) e191–e203.
[2] E. Heitzer, S. Perakis, J.B. Geigl, M.R. Speicher, The potential of liquid biopsies for the early detection of cancer, NPJ Precis. Oncol. 1 (2017) 1–9.
[3] A. Soni, C.M. Pandey, S. Solanki, G. Sumana, Synthesis of 3D-coral like polyaniline nanostructures using reactive oxide templates and their high performance for ultrasensitive detection of blood cancer, Sens. Actuators, B 281 (2019) 634–642.
[4] P.R. Srinivas, B.S. Kramer, S. Srivastava, Trends in biomarker research for cancer detection, Lancet Oncol. 2 (2001) 698–704.
[5] A. Khanmohammadi, A. Aghaie, E. Vahedi, A. Qazvini, M. Ghanei, A. Afkhami, A. Hajian, H. Bagheri, Electrochemical biosensors for the detection of lung cancer biomarkers: a review, Talanta 206 (2020) 120251.
[6] S.K. Arya, K.Y. Wang, C.C. Wong, A.R.A. Rahman, Anti-EpCAM modified LC-SPDP monolayer on gold microelectrode based electrochemical biosensor for MCF-7 cells detection, Biosens. Bioelectron. 41 (2013) 446–451.
[7] S. Tiwari, P.K. Gupta, Y. Bagbi, T. Sarkar, P.R. Solanki, L-cysteine capped lanthanum hydroxide nanostructures for non-invasive detection of oral cancer biomarker, Biosens. Bioelectron. 89 (2017) 1042–1052.
[8] A. Soni, C.M. Pandey, S. Solanki, R.K. Kotnala, G. Sumana, Electrochemical genosensor based on template assisted synthesized polyaniline nanotubes for chronic myelogenous leukemia detection, Talanta 187 (2018) 379–389.
[9] U. Schnell, V. Cirulli, B.N. Giepmans, EpCAM: structure and function in health and disease, Biochimica et Biophys. Acta (BBA)-Biomembranes 1828 (2013) 1989–2001.
[10] M. Munz, P.A. Baeuerle, O. Gires, The emerging role of EpCAM in cancer and stem cell signaling, Cancer Res. 69 (2009) 5627–5629.
[11] P.T.H. Went, A. Lugli, S. Meier, M. Bundi, M. Mirlacher, G. Sauter, S. Dirnhofer, Frequent EpCam protein expression in human carcinomas, Hum. Pathol. 35 (2004) 122–128.
[12] F.G. Ortega, M.A. Fernández-Baldo, M.J. Serrano, G.A. Messina, J.A. Lorente, J. Raba, Epithelial cancer biomarker EpCAM determination in peripheral blood samples using a microfluidic immunosensor based in silver nanoparticles as platform, Sens. Actuators, B 221 (2015) 248–256.
[13] J. Shi, J. Lyu, F. Tian, M. Yang, A fluorescence turn-on biosensor based on graphene quantum dots (GQDs) and molybdenum disulfide (MoS_2) nanosheets for epithelial cell adhesion molecule (EpCAM) detection, Biosens. Bioelectron. 93 (2017) 182–188.
[14] L. Tao, K. Zhang, Y. Sun, B. Jin, Z. Zhang, K. Yang, Anti-epithelial cell adhesion molecule monoclonal antibody conjugated fluorescent nanoparticle biosensor for sensitive detection of colon cancer cells, Biosens. Bioelectron. 35 (2012) 186–192.
[15] M.J. Shiddiky, S. Rauf, P.H. Kithva, M. Trau, Graphene/quantum dot bionanoconjugates as signal amplifiers in stripping voltammetric detection of EpCAM biomarkers, Biosens. Bioelectron. 35 (2012) 251–257.
[16] A.P.F. Turner, Biosensors: sense and sensibility, Chem. Soc. Rev. 42 (2013) 3184–3196.
[17] D. Grieshaber, R. MacKenzie, J. Vörös, E. Reimhult, Electrochemical biosensors - sensor principles and architectures, Sensors (Basel) 8 (2008) 1400–1458.
[18] H.J. Yoon, T.H. Kim, Z. Zhang, E. Azizi, T.M. Pham, C. Paoletti, J. Lin, N. Ramnath, M.S. Wicha, D.F. Hayes, Sensitive capture of circulating tumour cells by functionalized graphene oxide nanosheets, Nat. Nanotechnol. 8 (2013) 735–741.
[19] X. Chia, A.Y.S. Eng, A. Ambrosi, S.M. Tan, M. Pumera, Electrochemistry of nanostructured layered transition-metal dichalcogenides, Chem. Rev. 115 (2015) 11941–11966.
[20] K. Kalantar-zadeh, J.Z. Ou, Biosensors based on two-dimensional MoS_2, ACS Sensors 1 (2016) 5–16.
[21] H. Zhang, S. Lu, J. Zheng, J. Du, S. Wen, D. Tang, K. Loh, Molybdenum disulfide (MoS_2) as a broadband saturable absorber for ultra-fast photonics, Opt. Express 22 (2014) 7249–7260.
[22] K.-J. Huang, L. Wang, J. Li, Y.-M. Liu, Electrochemical sensing based on layered MoS_2–graphene composites, Sens. Actuators, B 178 (2013) 671–677.
[23] S. Jayabal, G. Saranya, J. Wu, Y. Liu, D. Geng, X. Meng, Understanding the high-electrocatalytic performance of two-dimensional MoS_2 nanosheets and their composite materials, J. Mater. Chem. A 5 (2017) 24540–24563.
[24] A. Soni, C.M. Pandey, M.K. Pandey, G. Sumana, Highly efficient Polyaniline-MoS2 hybrid nanostructures based biosensor for cancer biomarker detection, Anal. Chim. Acta 1055 (2019) 26–35.
[25] Y.J. Tang, Y. Wang, X.L. Wang, S.L. Li, W. Huang, L.Z. Dong, C.H. Liu, Y.F. Li, Y.Q. Lan, Molybdenum disulfide/nitrogen-doped reduced graphene oxide nanocomposite with enlarged interlayer spacing for electrocatalytic hydrogen evolution, Adv. Energy Mater. 6 (2016) 1600116.
[26] K. Chang, W. Chen, l-Cysteine-assisted synthesis of layered MoS_2/graphene composites with excellent electrochemical performances for lithium ion batteries, ACS Nano 5 (2011) 4720–4728.
[27] B. He, L. Chen, M. Jing, M. Zhou, Z. Hou, X. Chen, 3D MoS_2-rGO@Mo nanohybrids for enhanced hydrogen evolution: the importance of the synergy on the Volmer reaction, Electrochim. Acta 283 (2018) 357–365.
[28] F. Chekin, F. Teodorescu, Y. Coffinier, G.-H. Pan, A. Barras, R. Boukherroub, S. Szunerits, MoS_2/reduced graphene oxide as active hybrid material for the electrochemical detection of folic acid in human serum, Biosens. Bioelectron. 85 (2016) 807–813.
[29] Y. Chen, Y. Li, D. Deng, H. He, X. Yan, Z. Wang, C. Fan, L. Luo, Effective immobilization of Au nanoparticles on TiO_2 loaded graphene for a novel sandwich-type immunosensor, Biosens. Bioelectron. 102 (2018) 301–306.
[30] C.M. Pandey, G. Sumana, I. Tiwari, Copper oxide assisted cysteine hierarchical structures for immunosensor application, Appl. Phys. Lett. 105 (2014) 103706.
[31] W.S. Hummers Jr, R.E. Offeman, Preparation of graphitic oxide, J. Am. Chem. Soc. 80 (1958) 1339.
[32] J. Chen, B. Yao, C. Li, G. Shi, An improved Hummers method for eco-friendly synthesis of graphene oxide, Carbon 64 (2013) 225–229.
[33] D. Chen, L. Li, L. Guo, An environment-friendly preparation of reduced graphene oxide nanosheets via amino acid, Nanotechnology 22 (2011) 325601.
[34] O. Jalil, C.M. Pandey, D. Kumar, Electrochemical biosensor for the epithelial cancer biomarker EpCAM based on reduced graphene oxide modified with nanostructured titanium dioxide, Microchim. Acta 187 (2020) 275.
[35] L. Zheng, D. Ye, L. Xiong, J. Xu, K. Tao, Z. Zou, D. Huang, X. Kang, S. Yang, J. Xia, Preparation of cobalt-tetraphenylporphyrin/reduced graphene oxide nanocomposite and its application on hydrogen peroxide biosensor, Anal. Chim. Acta 768 (2013) 69–75.
[36] J. He, P. Li, W. Lv, K. Wen, Y. Chen, W. Zhang, Y. Li, W. Qin, W. He, Three-dimensional hierarchically structured aerogels constructed with layered MoS_2/graphene nanosheets as free-standing anodes for high-performance lithium ion batteries, Electrochim. Acta 215 (2016) 12–18.
[37] Y. Liu, Y. Zhao, L. Jiao, J. Chen, A graphene-like MoS_2/graphene nanocomposite as a highperformance anode for lithium ion batteries, J. Mater. Chem. A 2 (2014) 13109–13115.
[38] K. Chang, W. Chen, Single-layer MoS 2/graphene dispersed in amorphous carbon: towards high electrochemical performances in rechargeable lithium ion batteries, J. Mater. Chem. 21 (2011) 17175–17184.
[39] R. Vinoth, I.M. Patil, A. Pandikumar, B.A. Kakade, N.M. Huang, D.D. Dionysios, B. Neppolian, Synergistically enhanced electrocatalytic performance of an N-doped graphene quantum dot-decorated 3D MoS_2–graphene nanohybrid for oxygen reduction reaction, ACS Omega 1 (2016) 971–980.
[40] A. Bahuguna, S. Kumar, V. Sharma, K.L. Reddy, K. Bhattacharyya, P. Ravikumar, V. Krishnan, Nanocomposite of MoS2-RGO as facile, heterogeneous, recyclable, and highly efficient green catalyst for one-pot synthesis of indole alkaloids, ACS Sustain. Chem. Eng. 5 (2017) 8551–8567.
[41] A. Kaushik, P.R. Solanki, K. Kaneto, C.G. Kim, S. Ahmad, B.D. Malhotra, Nanostructured iron oxide platform for impedimetric cholesterol detection, Electroanalysis 22 (2010) 1045–1055.
[42] J.E.B. Randles, Kinetics of rapid electrode reactions, Discuss. Faraday Soc. 1 (1947) 11–19.
[43] J.-B. Jorcin, M.E. Orazem, N. Pébère, B. Tribollet, CPE analysis by local electrochemical impedance spectroscopy, Electrochim. Acta 51 (2006) 1473–1479.
[44] Y. Xie, A. Chen, D. Du, Y. Lin, Graphene-based immunosensor for electrochemical quantification of phosphorylated p53 (S15), Anal. Chim. Acta 699 (2011) 44–48.
[45] S. Augustine, P. Kumar, B.D. Malhotra, Amine-functionalized MoO_3@RGO nanohybrid-based biosensor for breast cancer detection, ACS Appl. Bio Mater. 2 (2019) 5366–5378.

[46] S. Verma, P. Arya, A. Singh, J. Kaswan, A. Shukla, H.R. Kushwaha, S. Gupta, S.P. Singh, ZnO-rGO nanocomposite based bioelectrode for sensitive and ultrafast detection of dopamine in human serum, Biosens. Bioelectron. 112347 (2020).
[47] Q. Chen, W. Hu, B. Shang, J. Wei, L. Chen, X. Guo, F. Ran, W. Chen, X. Ding, Y. Xu, Ultrasensitive amperometric aptasensor for the epithelial cell adhesion molecule by using target-driven toehold-mediated DNA recycling amplification, Microchim. Acta 185 (2018) 202.
[48] K. Bravo, F.G. Ortega, G.A. Messina, M.I. Sanz, M.A. Fernández-Baldo, J. Raba, Integrated bio-affinity nano-platform into a microfluidic immunosensor based on monoclonal bispecific trifunctional antibodies for the electrochemical determination of epithelial cancer biomarker, Clin. Chim. Acta 464 (2017) 64–71.